Size-Dependent Photocatalytic Activity of Silver Nanoparticles Embedded in ZX-Bi Zeolite Supports

Houeida Issa Hamoud, Fatima Douma, Mama Lafjah, Fatiha Djafri, Oleg Lebedev, Valentin Valtchev, Mohamad El-Roz

Size-Dependent Photocatalytic Activity of Silver Nanoparticles Embedded in ZX-Bi Zeolite Supports

*Houeida Issa Hamoud[‡a], Fatima Douma[‡a,b], Mama Lafjah[b], Fatiha Djafri[b], Oleg Lebedev[c], Valentin Valtchev[a], Mohamad El-Roz[a]**

[a]Laboratoire Catalyse et Spectrochimie, Normandie Université, ENSICAEN, UNICAEN, CNRS, 14050 Caen, France.
[b]Université d'Oran 1, Laboratoires de Chimie des Matériaux, 31039 Oran, Algeria.
[c]Labortoire CIMAP, Normandie Université, ENSICAEN, UNICAEN, CNRS, 14050 Caen, France.

Abstract

In this study, the photocatalytic activity of highly dispersed silver embedded into ZX-Bi zeolite during methanol photooxidation under visible light and at room temperature is investigated. The size and dispersion of $Ag_n^{\delta+}$ sub-nanoclusters (< 1 nm) is studied by HR/TEM, DR-UV-Vis, *in situ* FTIR, etc. The catalytic tests were performed using the operando FTIR technique during methanol photooxidation as a model reaction. The results show that the as-prepared Ag/ZX-Bi was very low active, while the activated sample at 200 °C (Ag/ZX-Bi_200) exhibits the highest photocatalytic activity (49.60 $mmol.g^{-1}.cm^{-2}$ after 12 h of reaction) during methanol photooxidation, more than 6 times higher than the TiO_2-P25 used as reference. This activity originates from the migration and agglomeration of sub-nanosized $Ag_n^{\delta+}$ clusters into Ag nanoparticles with a size of 6 nm. However, the catalyst experienced a partial desactivation when the particle size of sintered Ag NPs is below 20 nm. The activity and the deactivation of Ag/ZX-Bi will be discussed on the basis of operando FTIR results and HRTEM analysis at different stages of the reaction.

Keywords: Silver nanoparticles, Size effect, Plasmonic catalyst, Photocatalysis, Operando.

1. Introduction

The light-harvesting ability and the overall efficiency of a photocatalyst is highly dependent on its optical and electronic properties. Therefore, a good photocatalyst should ideally have i) a rapid response in the visible range for the maximum utilization of sunlight, ii) an efficient electron-hole separation, and iii) an efficient photogenerated electron and hole (e/h) transfer to the surface. Much of the efforts towards achieving these properties over the past decade have been focused on semiconductor photocatalysts by dispersing the semiconductor on various supports, coupling one or more semiconductors (hetero-junction systems), or by doping the semiconductor with metal nanoparticles [1,2]. Lately, noble metal nanoclusters (NCs) and nanoparticles (NPs), such as gold (Au) and silver (Ag), have been increasingly explored as alternative materials [3]. Noble metal nanoparticles (MNPs), are expected to provide a promising platform to design photocatalysts with high activities due to the ultrasmall size of metal NCs, which could shorten the distance of electron transfer from the metal NCs to the reactants. The large surface area related to the higher surface-to-volume ratios, the low bandgap, and the presence of reduced noble metal atoms prohibits the capture of the generated electrons or holes by the ions of the crystal, as in the case of the semiconductors. On the other hand, MNPs proved ability as a single catalyst in the plasmon-catalyzed reactions. The latter can be driven by the plasmon-resonant effect (LSPR), i.e., coherent oscillations of the conduction electrons of a particle with a size similar or smaller than the wavelength of light excitation under visible and NIR irradiations to generate charge carriers. Surface plasmon resonance can drive photocatalysis through two main pathways: direct and indirect. In the direct mode, the plasmonic nanoparticles, isolated or confined in photochemically inert supports such as zeolites, act both as light absorbers and as active sites for photocatalysis. In the indirect mode, the plasmonic nanostructures supported on semiconductors can transfer the

photon energy generated by the LSPR excitation to the semiconductor. The role of plasmonic metals is mainly related to the type of semiconductor and the irradiation light. For example, plasmonic metals can act as a photosensitizer under UV irradiation or as a co-catalyst under visible light [4]. The MNPs can drive reactions by visible light (e.g., activations of H_2 and O_2) that seem to be, in the view of conventional photochemical/thermal or electrochemical reactions, unachievable at mild conditions [5,6,7,8]. The action mode of MNPs can follow three different pathways: i) nonradiative Landau damping (also known as indirect charge transfer), ii) chemical interface damping (CID) with a weakly adsorbed substrate (Direct charge transfer), and iii) direct photoexcitation of the hybridized substrate–adsorbate bond. These mechanistic pathways are responsible for plasmon-enhanced photocatalysis either through localized heating or by generating energetic charge-carriers to reactants adsorbed on the NPs surface.

Plasmonic Ag NPs have attracted much attention because they have more powerful electromagnetic fields than other plasmonic metals (Au and Cu) [9,10,11]. Downsizing Ag NPs to an atomic level may maximize the fraction of accessible active sites during the photocatalytic reaction. Nevertheless, due to the high surface energy of ultrasmall metallic clusters, it is always challenging to maintain high dispersion as they are susceptible to agglomerate. Zeolite materials with their regular system of pore and cavities can provide a unique hosting environment for the construction of metallic clusters. The zeolites supports can also offer the advantage of the strong electric field strength which inhibit the e/h charge recombination via distribution of photogenerated electrons inside zeolitic network [12]. However, the zeolite-supported clusters frequently suffer from sintering under the thermal reaction conditions, which manifests by the migration and agglomeration of metallic species on the external surface of the zeolite. Recently, Monpezat et *al.* [13] quantified the sintering process and found that the micropores can only

prevent the migration and the coalescence of silver particles with a diameter > 0.5 nm. Moreover, a large fraction of silver nanoparticles (more than 85 %) is subjected to sintering at high temperatures.

In general, the photocatalytic performance depends strongly on the size of metal nanoparticles when used as co-catalyst. However, it is impossible to make a general conclusion on the evolution of the reaction activity as function of the size of metallic species when this later is used as photocatalyst. In some reactions, isolated atoms and clusters are more active than the nanoparticles, while in others the metal clusters represent the active sites but not the nanoparticles. For example, Santillán et *al.* [14] demonstrated strong size-dependent photocatalytic properties over few atoms of silver clusters. The authors showed that a small Ag cluster containing few atoms (0.1-1.5 nm) displayed higher activity in methylene blue photodegradation compared to a highly fluorescent Ag NPs (250-300 atoms). In contrast, Li et *al.* [15] showed that $Ag/SiO_2/Pt$ heterostructures with Ag NPs in an intermediate size range of 25 and 50 nm diameter exhibited plasmon-enhanced photocatalytic performance four times larger than for smaller NPs (≤12 nm diameter). It was shown that when the size of Ag is in the range (25-50 nm), the incident photons generate intense local fields. However, when particle size is small than 12 nm, the effective absorption section decreases, minimizing the local field enhancement and reducing the photocatalytic activity.

Recently, we developed a new approach for embedding silver clusters and quasi-nanoparticles in zeolite and investigating their optical and plasmonic properties [16]. This work will be dedicated to explore the photocatalytic activity and stability of the prepared materials (Ag/ZX-Bi) as well as the effect of the different activation process on the photocatlytic performance. The photocatalytic oxidation of methanol at RT under visible irradiation was used as a model reaction. First, the

physicochemical properties of the silver-free (ZX-Bi) and silver-containing (Ag/ZX-Bi) zeolites were studied by different techniques such as XRD, N_2 physisorption at 77K, DR-UV-Vis and TEM will be presented. Then, the photocatalytic activity was investigated under visible light and different conditions of thermal activation. Finally, the mechanism governing the photocatalytic activity and the deactivation process was addressed.

2. Experimental part

2.1. Catalyst synthesis

Sub-nanometer silver clusters embedded nanosized zeolites ZX-Bi (FAU-type, 10-30 nm, Si/Al = 1.63) were prepared in two steps (scheme 1), using the same procedure described by Douma et *al.* [16]. In the first step, the nanosized ZX-Bi was synthesized from a clear precursor suspension with the following molar composition: 10 SiO_2: 1.1 Al_2O_3: x Bi: 9 Na_2O: 122 H_2O (x = 0.24 equivalent to 3 wt. % of Bi in respect to (Si+Al)). The initial reactants were mixed to prepare two initial solutions denoted A and B. Solution A was prepared by dissolving 0.298 g of aluminum powder (325 mesh, 99.5%, Alfa Aesar) and 0.5 g of NaOH (Aldrich, 97%) in 3 mL of double-distilled water. Bismuth-containing samples were prepared by adding 0.118 g of $Bi(NO_3)_3.5H_2O$ to this solution and sonicated for 30 min to dissolve the $Bi(NO_3)_3$ completely. Solution B was prepared by mixing 10 g colloidal silica (Ludox-AS 30, Aldrich) with 1 g of NaOH and 1 mL of double-distilled water. The resulting suspensions were treated at 90 °C for 7 minutes to obtain a water-clear suspension. Solution A was added dropwise under vigorously stirring to the solution B in an ice bath. The resulting colorless suspensions were stirred at RT for 24 h, then freeze-dried and crystallized at 50 °C for 24 h. The nano-particles of ZX-Bi was recovered by centrifugation (25 min, 20000 rpm) followed by redispersion in double-distilled water. The procedure was repeated till reaching pH ~ 8. The second step was devoted to the preparation of Ag/ZX-Bi by

dispersing ZX-Bi (zeolite concentration=2.4 mg/ml) in a water/ethanol mixture (water:ethanol = 3:1; 20 ml) that contained silver nitrate (10^{-2} M). The reduction of silver ions is performed by a photo-assisted redox reaction under UV irradiation for 5 min under stirring using a polychromatic Hg-Xe lamp (polychromatic irradiance = 205 mW/cm^2; infrared cut filter). Upon irradiation the color of the suspension changed from milky to magenta, confirming the reduction of silver Ag_n^{n+} to $Ag_n^{\delta+}$ clusters (with $\delta<n$). More details concerning the mechanism of the silver reduction and samples analysis can be found in reference [16]. The Ag/ZX-Bi solid was recovered using the same procedure described in step 1, followed by drying at 50 °C under air atmosphere.

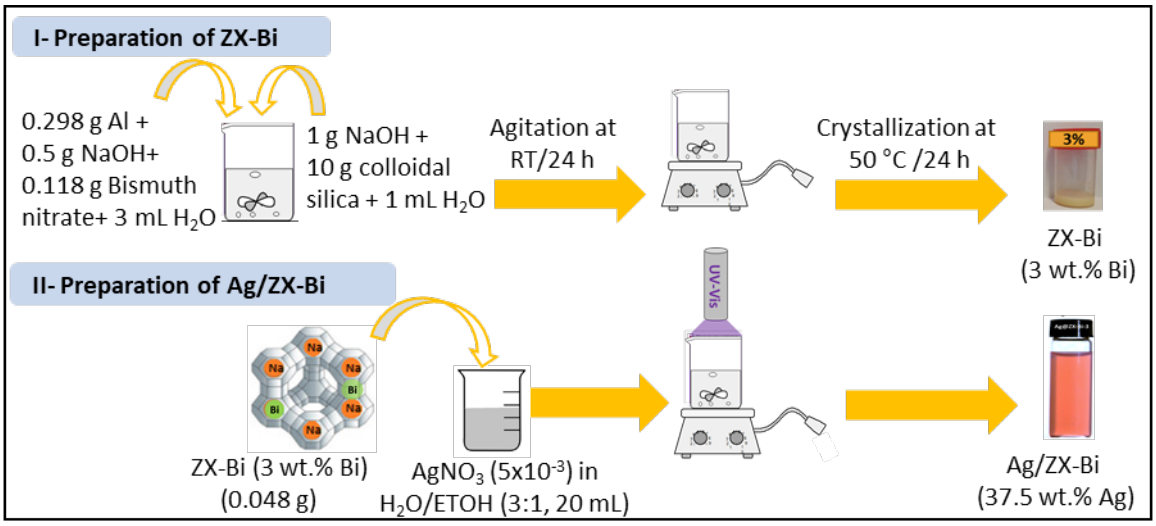

Scheme 1. Schematic illustration representing the step-by-step synthesis process of ZX-Bi and Ag/ZX-Bi.

2.2. Physicochemical analyses

X-Ray Diffraction (XRD) analysis of the ZX-Bi and Ag/ZX-Bi materials were carried out with PANalyticalX'Pert Pro diffractometer with CuKα irradiation (λ = 1.5418 Å). The PXRD diagrams were recorded at room temperature between 5 and 50° (2θ) with a step size of ~0.014°. Variable divergent slits with a constant illuminated sample length of 6 mm were used. Phase identifications were performed with the PANalytical High Score plus program.

Nitrogen adsorption/desorption measurements were performed with an ASAP 2020 MP instrument. The specific surface area was calculated with the BET equation, while the pore volumes were determined by the BJH method. Prior to the measurements, samples were *in-situ* outgassed at 200 ºC for 3 h.

The X-ray photoelectron spectroscopy (XPS) measurements have been performed with an AXIS Supra electron spectrometer (Kratos Analyical Ltd.) equipped with a monochromatized Al Kα radiation (1486.6 eV). For all analyses, the take-off angle of the photoelectrons was 180°. High-resolution spectra of the C 1s, Si 2p, Al 2p, Na 2s, O 1s, Ag 3d, and Bi 4f core-level regions were recorded with a pass energy of 20 eV. Due to the important surface charging effect, a resolution of ~1.0 eV has been measured on the samples. Binding energy is referred to the C 1s peak at 284.6 eV (hydrocarbon from contamination). The XPS analysis was performed at ambient temperature and under vacuum (10^{-8} Pa).

DR-UV-Vis measurements relevant to Ag's speciation and oxidation state were carried using a Cary 4000 UV-Vis spectrophotometer and a HARRICK praying Mantis diffuse reflectance accessory. All spectra were recorded between 200-800 nm using an average time of 0.2 s and a scan rate of 300 nm/min.

Advanced transmission electron microscopy (TEM) was carried out on an aberration probe, and image corrected JEM ARM200F cold FEG microscope operated at 200 kV equipped with a CENTURIO EDX detector and GIF Quantum spectrometer.

In-situ FTIR spectroscopy on chemisorption of CO was performed at low temperature (- 173 ° C) in order to determine the nature and the oxidation state of silver active sites and their accessibility. The samples (pellet of ~20 mg) were first heated under vacuum ($<10^{-6}$ mbar) at 100 °C for 18 h. The samples were then saturated by a 1 dose equilibrium of CO (20 torr). The IR

spectra were recorded with a Nicolet 6700 FTIR spectrometer equipped with a DTGS detector at a spectral resolution of 4 cm^{-1} by accumulating 128 scans.

The transient absorption spectra and the kinetic decay of the samples were recorded on LP980 laser flash photolysis instrument (Edinburgh, UK) equipped with a 5-10 ns pulsed Nd-YAG laser (266, 355, 532, and 1064 nm) (Q-smart 450 10Hz 2W3W4W).

The formation of reactive species over Ag/ZX-Bi_200 catalyst was evidenced by the fluorescence quenching method using 1,3-diphenylisobenzofuran described in reference [17]. In the experimental set-up, the probe 1,3 diphenylisobenzofuran (DPBF, 10^{-5} M in n-heptane) was added to 1.5 mg/mL of catalyst dispersed in n-heptane.The solution was prepared in a closed quartz cuvette with a screw caps (1 cm optical length) and bubbled for 10 min under argon or oxygen prior to irradiation. Irradiations were performed at 405 nm using a LED-light source. The reaction of the fluorescent probe, diphenylisobenzofuran, with reactive oxygen is leads first to an intermediate which is then converted to the non-fluorescent o-dibenzoylbenzene (DBB) (see SI, scheme S1). Therefore, the concentration of DPBF was followed by fluorescence, λ_{ex} = 410 nm and λ_{em}= 454 nm using a FS5 Spectrofluorometer with TCSPC laser (Edinburgh Instruments). Noting that the analysis are only qualitative due to the low dispersion of the catalyst in n-heptane.

2.3. Photocatalytic test

For the operando experiments, a 'sandwich like' IR cell-reactor was used to study the performance of ZX-Bi and Ag/ZX-Bi catalysts during methanol photooxidation [18,19]. First, the catalyst (shaped as a pellet, $m_{catalyst}$~ 20 mg) was pretreated at room temperature under Ar and visible irradiations using a Xe-lamp (LC8 Hamamatsu, 71 mW/cm^2 of irradiance) with a pass-high filter >390 nm, followed or not by thermal treatment at 120 °C or 200 °C for 30 min in dark and 30 min

under visible irradiation with a heating rate of 2 °C.min^{-1}. Then, the reaction was studied at room temperature (T = 25 °C) in the presence of methanol ([MeOH]$_0$ = 2100 or 10350 ppm) and 20% of O_2 in Ar with a total flow rate of 25 cc.min^{-1}. It should be noted that the TiO_2 P25 benchmark (Evonic-Degussa) was also tested under similar conditions and considered as a reference. The relative concentrations of the effluent gas were stabilized before being sent to the cell, then an adsorption step of methanol on the catalyst surface was performed in dark before turning on the lamp. Finally, the composition of the output gas from the IR reactor cell was analyzed simultaneously by Mass Spectrometry (Quadrupole Pfeiffer Omnistar GSD 301) and IR spectrometer (ThermoNicolet NEXUS 670 FTIR) equipped with an MCT detector with a spectral resolution of 4 cm^{-1} and accumulating 64 scans. A calibration curve was drawn to establish the linear relationship between the concentration of methanol and the IR band area (at 1038−1026 cm^{-1}) and MS signal (m/z = 29). The concentration of MeOH was determined at the steady-state of the reaction, when no more changes in both the MS signals and the IR spectra were observed depending on the catalyst type. Selectivity of CO_2 was determined using the IR band area at 2395-2182 cm^{-1} and the MS signal at m/z = 44. The amounts of formaldehyde (FA) and methyl formate (MF) were determined after deconvolution of the IR spectrum of the gas phase, at the steady-state, during the methanol photooxidation over TiO_2-P25 after proportional subtraction of water, water and formaldehyde, and water and methyl formate vibration bands, respectively. The selectivity was determined using the IR band areas at 1750-1758 and 1757-1750 cm^{-1} for FA and MF, respectively. More technical details can be found in references [18] and [19].

The methanol conversion (expressed in % or in mmol per g of photocatalyst per irradiated surface) and the selectivity (in %) were calculated from equations 1-3, at the steady-state using the calibration curve for different products of the reaction. It should be noted that the irradiated surface

($S_{irradiated}$) of the pellet is about 1.6 cm^2 (~ 20 % of the outer surface is not irradiated since the visible irradiation cannot reach the total surface of the pellet due to the shading of metallic holder used for fixing the sample in the reactor). The methanol conversion and conversion yield are calculated as following:

$$\text{MeOH conversion (\%)} = \frac{[\text{MeOH}]_0\ (ppm) - [\text{MeOH}]_t\ (ppm)}{[\text{MeOH}]_0\ (ppm)}\ \text{x}\ 100 \quad (1)$$

$$\text{Conversion Yield (mmol.}\ g^{-1}.\ cm^{-2}) = \frac{\text{Total flow}(cc.min^{-1})\ \text{x}\ 10^3\ [\text{MeOH}]0\ (\text{ppm})\ \text{x}10^6\text{x}\ \frac{\text{conversion \%}}{100}\text{x t (min)}\ \text{x}\ 1000}{V_m(L.mol^{-1})\ \text{x}\ m_{catalyst}(g)\ \text{x}\ S_{irradiated}(cm^2)} \quad (2)$$

, With V_m = molar volume = 24 $L.mol^{-1}$.

$$\text{Selectivity (\%)} = \frac{\text{Concentration of target product (ppm)}}{\text{Concentration of methanol converted (ppm)}}\ \text{x}\ 100 \quad (3)$$

3. Results and Discussion

3.1. Characterization of ZX-Bi and Ag/ZX-Bi catalysts

In this section, the physico-chemical properties of ZX-Bi and Ag/ZX-Bi will be briefly presented. For more details, please refer to the cited reference therein [16]. The X-ray diffraction patterns of the ZX-Bi and Ag/ZX-Bi samples are shown in Fig. S1(A). The ZX-Bi sample shows the typical structure of FAU-type zeolite according to the literature [20] (with characteristic lines at 2-Theta = 6.19; 10.31; 11.95; 15.86; 23.82; 26.86 and 31. 2°) indicating that the synthesized crystal is pure FAU zeolite without any evidence of the presence of crystalline Bi oxide. A significant change in the relative intensities of the diffraction peaks can be observed after Ag loading into the ZX-Bi structure, which is mainly related to the differences in the charge balancing cation composition of two samples. However, the XRD patterns of Ag/ZX-Bi do not display any evidence of metal or metal oxide (M_xO) phases (M = Ag), suggesting that the silver species (8.6 at. % as detected by XPS, see Table 1) exist in highly dispersed states and/or with low particle size.

Concerning the textural properties (Fig. S1(B)), both ZX-Bi and Ag/ZX-Bi samples exhibit a combination of Type I and IV isotherms with an H1-type hysteresis. The surface areas and the total pore volumes of ZX-Bi and Ag/ZX-Bi samples are summarized in Table 1. A significant decrease in the specific surface area (35%) and the total pore volume (32%) is observed after loading of silver in the ZX-Bi structure. This significant decrease can be attributed in part to the higher atomic weight of silver particles compared to the sodium initially present as counter-ions in the ZX sample, in addition to the zeolite pore occupation by silver particles. The XPS analysis shows that Bi^{2+} and Bi^{3+} coexisted in the ZX-Bi sample with an atomic ratio around 0.7 (Bi^{2+}/Bi^{3+}), while the Bi^{5+} was the only bismuth species detected in Ag/ZX-Bi, confirming a photo-assisted redox reaction between the Bi^{2+}/B^{3+} and Ag^{+} to produce reduced silver clusters ($Ag_n^{\delta+}$).

Table 1. Textural and chemical properties of ZX-Bi and of as-prepared Ag/ZX-Bi.

Samples	S_{BET} (m2/g)	V_{total} (cm3/g)	Si (at. %)	Al (at. %)	Na (at. %)	O (at. %)	Ag (at. %)	Bi II (at. %)	Bi III (at. %)	Bi V (at. %)	Na/Al	Bi/Al
ZX-Bi	826.6	0.65	14.1	10.5	10.3	48.4	-	0.06	0.09	-	0.98	0.01
Ag/ZX-Bi	532.4	0.44	13.8	9.3	2.1	46.7	8.6	-	-	0.15	0.22	0.01

The DR-UV–Vis spectrum of Ag/ZX-Bi powder (Fig. S1(C)) demonstrates the appearance of new UV-Visible bands at 326, 367, 394, 460 and 525 nm. In the UV region, the bands at 326 and 394 nm are assigned to the formation of the silver nanoclusters $Ag_n^{\delta+}$ with $n \geq 7$. These species are formed by the connection of smaller clusters embedded in the sodalite cage through 6MR prism promoting the formation of quasi-nanoparticles [21,22]. The shoulder at 367 nm is assigned to the fingerprints of hydrated Ag_4^{2+} [23]. The presence of small ionic silver clusters was also confirmed by the *in situ* FTIR analysis using CO as a probe molecule at low temperature (Fig. S2). The bands in the visible region (at 460 and 525 nm), at the origin of the magenta color of the powder, are probably due to a strong interaction between the oxygen framework of zeolite (O_F) and the silver

clusters by a transitional charge transfer (CT) with a strong connection between the silver clusters in the neighboring zeolite cages [23,24]. The suggested interconnection between Ag sub-nanoparticles, with a typical diameter of about 1.0 nm, within the 6-member ring prism of FAU structure was confirmed by TEM images (Fig. S3). More details on the optical behavior of Ag/ZX-Bi can be found in reference [16].

3.2. Catalytic activity in methanol photooxidation

3.2.1. Choice of the experimental conditions

In our previous study [16], it was shown that the Ag/ZX-Bi was successfully prepared with a unique optical property and a particular plasmonic behavior leading to a local heating equivalent to 190°C under visible irradiation. The set of the analysis showed the formation of interconnected silver clusters (silver quasi-nanoparticles) through the zeolite channels. Due to these novel structural, electronic, and optical properties of Ag/ZX-Bi, the sample was employed as a photocatalyst. Thus, the Ag/ZX-Bi sample was tested during methanol photooxidation at 25 °C (RT) in gas phase under visible light irradiation. Each experiment was repeated at least two times with an estimated error of less than 10% for silver-based samples and 5% for TiO_2 P25 used as benchmark reference and tested under similar reaction conditions.

To select the optimum operating conditions, the effect of the activation temperature on the photocatalytic activity of Ag/ZX-Bi was initially investigated under flow reaction condition (25 $cc.min^{-1}$) in the presence of 10350 ppm (~1%) of MeOH under visible irradiation. The catalytic tests were performed on non-activated (as-prepared) and *in-situ* activated samples at 120 or 200 °C under argon, labelled as Ag/ZX-Bi_NA, Ag/ZX-Bi_120 and Ag/ZX-Bi_200, respectively. The methanol conversion yield (expressed in $mmol.g^{-1}.cm^{-2}$) as functions of irradiation time (min) are

shown in Figure 1(A). The results indicate that the Ag/ZX-Bi_NA has very low activity during the methanol photooxidation (5.94 $mmol.g^{-1}.cm^{-2}$; 2.7 % of MeOH conversion at t = 720 min), then the photocatalytic activity increases with increasing the tempertaure of calcination from 120 to 200 °C. The Ag/ZX-Bi_200 exhibits the highest photocatalytic activity with a maximum of 3.58 $mmol.g^{-1}.cm^{-2}$ corresponding to 57 % of MeOH conversion after 20 min of irradiation. Then, the Ag/ZX-Bi_200 was exposed to a slight deactivation process before reaching the steady-state as deduced from the change in the slope of the conversion curve and the decrease of the amount of converted methanol (Fig. 1A-Insert). After 12 hours of reaction (720 min), the conversion was around 49.6 $mmol.g^{-1}.cm^{-2}$ (Fig. 1A), and the methanol conversion stabilized at 20 % (Fig. 1A-Insert). This result suggests that the interconnected silver clusters (~ 1 nm of diameter) of Ag/ZX-Bi_NA are not active during MeOH photooxidation, while they become active after an *in-situ* activation at 200 °C, which probably induce significant changes in the nature and/or size of the active sites. However, the diffraction pattern of Ag/ZX-Bi remains intact after activation at 120 and 200 °C under Argon (Fig. S4), suggesting that the thermal treatment did not alter the catalyst structure or that the induced changes resulting from this treatment are below the detection limit of XRD. For the BET measurement, a pre-activation for 3 h under vacuum and at relatively high temperature (> 200 °C) is required to remove the physiosorbed water. However, the pre-activation at 120 °C (to estimate the surface area at 120 °C) is not enough as a part of this water is still present on the samples. As the zelolite is not active as support, the activity is more related with the particle size and/or to the accessibility of the active site. The comparison between 120 °C and 200 °C was to select the optimal activation condition for further investigation.

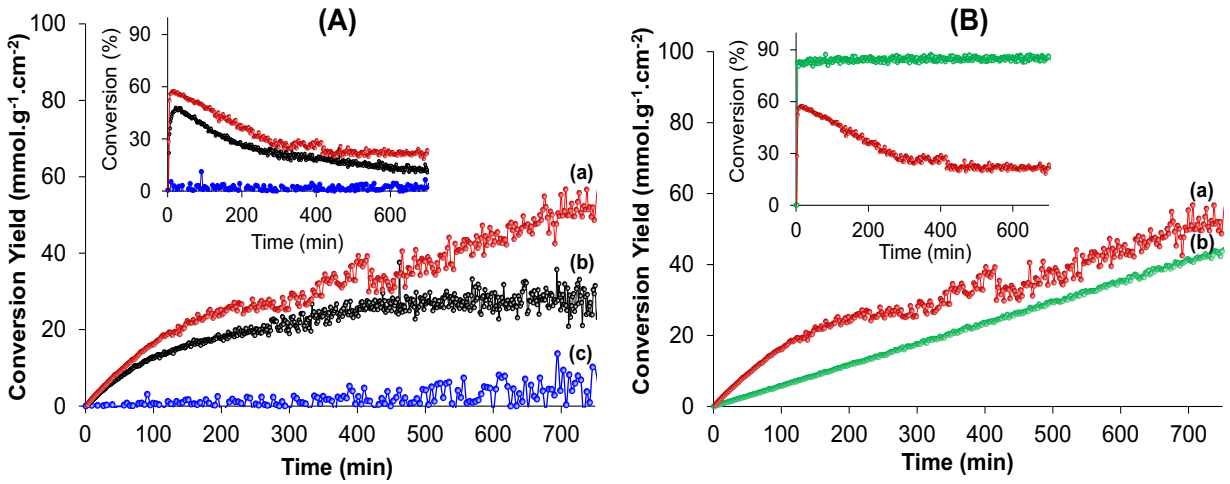

Figure 1. (A) Effect of the activation temperature on the photocatalytic activity of Ag/ZX-Bi (a) activated at 200 °C (Ag/ZX-Bi_200), (b) activated at 120 °C (Ag/ZX-Bi_120) and (c) non-activated (Ag/ZX-Bi_NA). (B) Effect of the MeOH initial concentration (a) 10350 ppm and (b) 2100 ppm on the photocatalytic activity of Ag/ZX-Bi_200. The insert corresponds to the methanol conversion in % as a function of reaction time. Reaction condition: [MeOH]=10350 (~1%) for A in 20%O_2/Ar; $m_{catalyst}$=20mg; Lampe Xe with filter pass high (λ>390nm); irradiance = 71 mW/cm^2; Total flow= 25 cm^3/min. Catalysts activated at 120 or 200 °C under Ar for 30 min in dark followed by 30 min under visible irradiation; heating rate = 2°C/min.

Due to the deactivation of Ag/ZX-Bi_200 in the presence of a high concentration of methanol (10350 ppm, ~1%), the reaction was performed at a relatively lower concentration corresponding to 2100 ppm (Fig. 1(B)). By decreasing the methanol concentration from 10350 to 2100 ppm, a total conversion (1.12 mmol.g^{-1}.cm^{-2} corresponding to 81% of MeOH conversion at t = 20 min) was observed without any significant deactivation (Fig. 1B-Insert). This is confirmed by the rapid vanishing of methanol IR band (1038-1026 cm^{-1}) from the gas phase after 2 min of irradiation and the simultaneous formation of CO_2 at 2395-2182 cm^{-1} as the only product (Fig. S5(A)). It should be noted that the total conversion of MeOH cannot reach 100%, since the outer surface of the pellet (about ~ 20 %) is not illuminated. Whatever the initial concentration of MeOH, the CO_2 (2395-2182 cm^{-1}) is still the only detected product in the gas phase even after 12 h of visible light irradiation (Fig. S5(A-B), indicating that the initial concentration of MeOH cannot affect the reaction selectivity. In the contrary, the selectivity of TiO_2 P25 is highly dependent on

the initial concentration of MeOH as shown by El-Roz et *al.* [25]. This is attributed to the coverage level of the TiO_2 P25 surface by the chemisorbed MeOH as surface methoxy groups. In addition to its poor selectivity, TiO_2 presents other disadvantages such as [26]: low surface area, poor adsorption, absorption in UV range and rapid e/h charge recombination that limit the application of TiO_2 in photocatalysis to favor of the proposed system in this work. More details about the reaction pathway over TiO_2 P25 will be discussed in the next section.

Finally, the effect of the aging time of the Ag/ZX-Bi photocatalyst on its performance was studied on fresh and aged Ag/ZX-Bi_200 samples for 3 and 12 months, respectively, and preactivated at 200°C (Fig. S6). The results show that the methanol conversion decreases with the aging time from 3 to 12 months. The conversion calculated after 180 min (3 h) of irradiation was found to be 24.67 $mmol.g^{-1}.cm^{-2}$ for the fresh sample, while lower values were obtained for the aged Ag/ZX-Bi_200 for 3 months (6.90 $mmol.g^{-1}.cm^{-2}$) and 12 months (2.31 $mmol.g^{-1}.cm^{-2}$), respectively (Fig. S6). Interestingly, after 12 months of aging time, the Ag/ZX-Bi_200 still showed similar activity to that observed for commercial TiO_2 P25, making it a potential candidate in photocatalysis of volatile organic compounds.

Given these results and to better understand the deactivation process, the catalytic tests in the next sections are performed in the presence of 10350 ppm (~1%) of initial concentration of methanol and on fresh samples that are *in-situ* activated at 200 °C under Argon.

An additional sample was prepared by Ag ionic exchange of ZX-Bi with silver cations and tested with and without *in-situ* activation at 200 °C under argon during methanol photooxidation. The two samples are labeled as IE-Ag/ZX-Bi_NA and IE-Ag/ZX-Bi_200, respectively (Fig. 2(A) and Fig. S7). In contrary to the IE-Ag/ZX-Bi_NA sample, which is completely inactive, the IE-

Ag/ZX-Bi_200 shows a catalytic behaviour similar to Ag/ZX-Bi_200 with 1.5 times lower activity during MeOH photooxidation. Hence, we anticipate that the thermal treatment of the IE-Ag/ZX-Bi sample at 200 °C promotes the reduction of silver cations in the presence of Bi^{2+}/Bi^{3+} via an electrochemical process. Furthermore, the reduction of Ag^{+} into silver nanoparticles by thermal treatment at 185 °C in the presence of a reducing agent under an inert atmosphere has been already reported in the literature [27]. Regardless of the preparation method, both Ag/ZX-Bi_200 and IE-Ag/ZX-Bi_200 samples were active in the methanol photooxidation, confirming the formation of similar active sites, but in different proportions during the thermal activation at 200 °C under argon. The significantly higher activity of Ag/ZX-Bi_200 in respect to IE-Ag/ZX-Bi_200 is probably related to the higher dispersion and smaller particle size of the generated silver nanoparticles. It should be noted that the commercial TiO_2 P25 was not affected by the thermal activation.

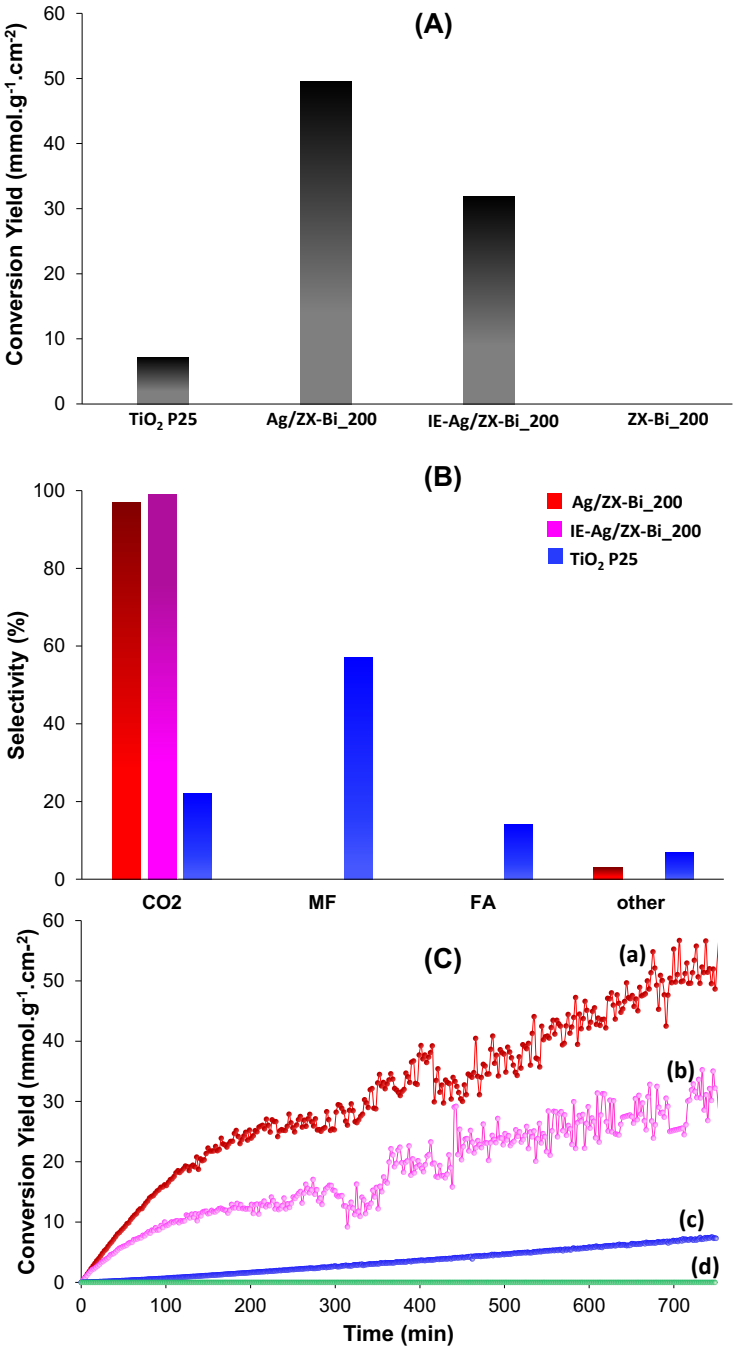

*

Figure 2. (A) Methanol conversion yield (in mmol per gram of catalyst per cm^2 of irradiated surface) and (B) selectivity (%) calculated at t = 720 min (~12h) of reaction and (C) evolution of the methanol conversion versus the irradiation time on (a) Ag/ZX-Bi_200, (b) IE-Ag/ZX-Bi_200, (c) TiO_2 P25 and (d) ZX-Bi_200 samples. Reaction conditions: [MeOH]= 10350 ppm in 20%O_2/Ar; $m_{catalyst}$=20mg; Lampe Xe with filter pass high (λ>390nm); irradiance = 71 mW/cm^2; Total flow= 25 cm^3/min. Catalysts activated at 200 °C under Ar for 30 min in dark followed by 30 min under visible irradiation; heating rate = 2°C/min.

As can be seen in Figures 2(A and C), the order of activities after 720 min (~12h) of reaction is the following: Ag/ZX-Bi_200 (49.60 mmol.g^{-1}.cm^{-2}) > IE-Ag/ZX-Bi_200 (31.90 mmol.g^{-1}.cm^{-2}) > TiO_2-P25 (7.18 mmol.g^{-1}.cm^{-2}) >>> ZX-Bi-200 (no activity). It is important to mention that the curves of CO_2 produced over the tested samples ideally follow the same profile as for the conversion curves of MeOH (Fig. S8). As expected, the parent ZX-Bi_200 was not active at all, and no CO_2 was detected in the outlet gas of this sample (Fig. S9), which is explained by the lack in the active species with absorption bands in the visible-light region (see DR-UV-Vis spectrum on Fig. S1(C)). This result confirms that the silver species in the ZX-Bi matrix are responsible for the observed photocatalytic activity. On the other hand, very interesting variations in the catalyst's selectivity were observed during methanol photooxidation for Ag/ZX-Bi_200 and IE-Ag/ZX-Bi_200 compared to the TiO_2 P25 (Fig. 2(B)). The former samples exhibited high selectivity towards CO_2 (> 97 %), while the commercial TiO_2 exhibited low selectivity. The percentage of carbon dioxide in the products of methanol photooxidation over P25 was found to be around 22 %. Other products were also detected in the outlet gas of TiO_2 P25 (Fig. S9-11) and attributed to the further transformation of methanol to methyl formate (~57 %), formaldehyde (~14 %), and other products (~7 %). According to the literature [19,25,28], the main pathway for methanol photooxidation over TiO_2 goes through the chemisorption of MeOH as surface methoxy species, then their oxidation into formate and finally CO_2. A parallel pathway is the formation of methylformate, as a secondary product, from a cross-coupling of a neighboring adsorbed formate and methoxy groups. At a high concentration of MeOH (10350 ppm, 1%), the formation of methylformate, as a secondary product, is favored by a high surface coverage of methoxy species. This explain the strong influence of methanol concentration on the reaction selectivity when TiO_2 P25 is used as photocatalyst.

To the best of our knoweldege, there is only one study on MeOH photo-oxidation in gas phase where Ag (with Au) are used as co-catalyst on TiO_2 as photocatalyst under UV irradiation [29**]**. Thus, we compare the performance of our system to TiO_2 P25 as the benchmark photocatalytic reference system. Based on the obtained results, one can stand that the Ag/ZX-Bi_200 is a promising candidate for MeOH photooxidation compared to TiO_2 P25 due to its high catalytic activity (49.60 $mmol.g^{-1}.cm^{-2}$ *vs.* 7.18 $mmol.g^{-1}.cm^{-2}$ for TiO_2) and selectivity (100 % of CO_2 selectivity vs. 22% for TiO_2 P25). Another advantage of using Ag/ZX-Bi_200 as photocatalyst is that the selectivity of reaction was independent of the initial cohindershindersncentration of MeOH, contrary to TiO_2 P25. However, the deactivation of this catalyst during the reaction is still a challenge that hinders its long-term use. Understanding catalyst's deactivation is the first step in developing a more resistant catalyst and/or an effective regeneration strategies. For this reason, in the next section, more profound analysis/characterization is performed to better understand the deactivation process of the catalyst during methanol photooxidation.

3.2.2. Photocatalyst deactivation

Operando IR analysis of the photocatalyst performed in the present study shed some light on the evolution of the surface species on Ag/ZX-Bi_200 during the reaction. The results are illustrated in Figure 3. After MeOH adsorption (spectrum a), new bands apperaed at 2952-2838 and 1450 cm^{-1} due to the strong asymmetric, symmetric and deformation vibrations of C-H bonds of methoxy species, repectively [19,30]. The bands located at around 2989 and 1476 cm^{-1} could be assigned to the stretching and bending vibration in methanol molecules weakly adsorbed on catalyst surface via hydrogen bonding interactions. Additionally, the band at 1640 cm^{-1} is attributed to the bending vibration of zeolitic water. Once the lamp is turned on (spectra b-d), a

fast disappearance of adsorbed methanol is observed in the first 10 min of reaction, accompanied by the regeneration of Si-OH, Si-OH-Al and-OH hydroxyl groups in the 3750-3500 cm^{-1} region [31]. It should be noted that the band observed at 2400-2280 cm^{-1} in the first 10 min is due to the interferences with the CO_2 produced in the gas phase with high concentration. In addition, new bands appeared at 1712 and 1372 cm^{-1} in the Ag/ZX-Bi_200 spectrum in the first minutes of irradiation that could be assigned to methyl formate/formate as surface intermediate species. However, these bands are totally disappeared after 4 minutes of reaction (see the zoom on Fig. 3), suggesting the rapid decomposition of methyl formate into CO_2 as no formic acid, formaldehyde, methylformate and/or CO are detected as final products in the gas phase. We did not detect other intermediates during methanol photooxidation over Ag/ZX-Bi_200 catalyst. This is either related to the rapid conversion of the intermediates to gas phase's products and/or that the oxidation of the methanol occurs in the gas phase. The latter hypothesis is supported by the fact that the reaction selectivity was independent of the MeOH concentration. However, a significant rising of the baseline is observed with the irradiation time (Fig. 3), which makes the exploitation of surface spectra impossible. This increase in the baseline intensity is due to Mie scattering effects in spectra, i.e., light scattering from large-sized particles [32]. Thus, the increase in the baseline intensity might be related to an increase in the Ag particle size of Ag/ZX-Bi_200 during the reaction.

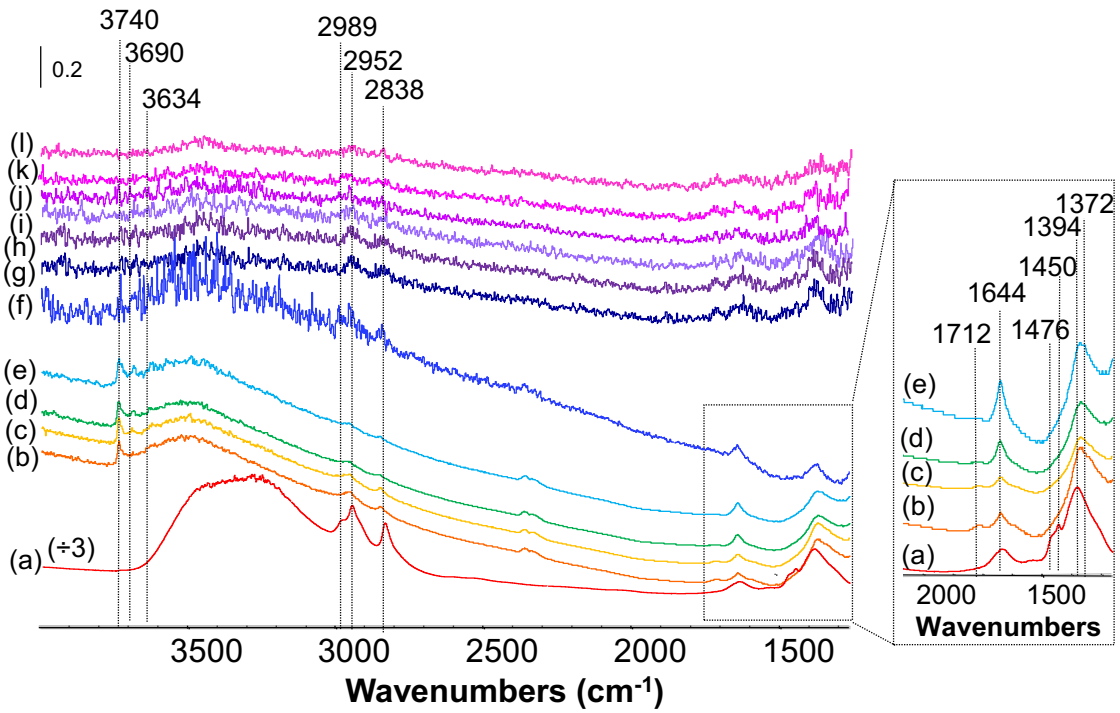

Figure 3. Evolution of the IR spectra of Ag@ZX-Bi_200 during the photooxidation of methanol during the first minutes of irradiation: (a) 0, (b) 2, (c) 4, (d) 6 , (e) 10 min and at prolonged time (f) 2, (g) 4, (h) 6, (i) 8,(j) 10, (k) 11 and (l) 12 h of visible light irradiation at 25 °C. on the right: zoom on the 1500-2000 cm^{-1} region of the catalyst surface in the first minutes of irradiation. reaction condition: MeOH=10350 ppm; 20%O_2/Ar; Lamp Xe (λ>390 nm); irradiance = 71 mW/cm^2; total flow=25 cm^3/min; m_{cat}=20 mg.

The question that arises now is whether the particle size of silver nanoclusters, initially with ~1 nm diameter, would change during the methanol photooxidation, as the case during the conventional thermal catalysis on plasmonic metal particles. To answer this question, Ag/ZX-Bi samples were ex-situ characterized by XRD, DR-UV-Vis and TEM after activation at 200 °C under Argon and at different photocatalytic reaction time (t = 1 h and 12 h). The results are shown in Figures 4 and 5.

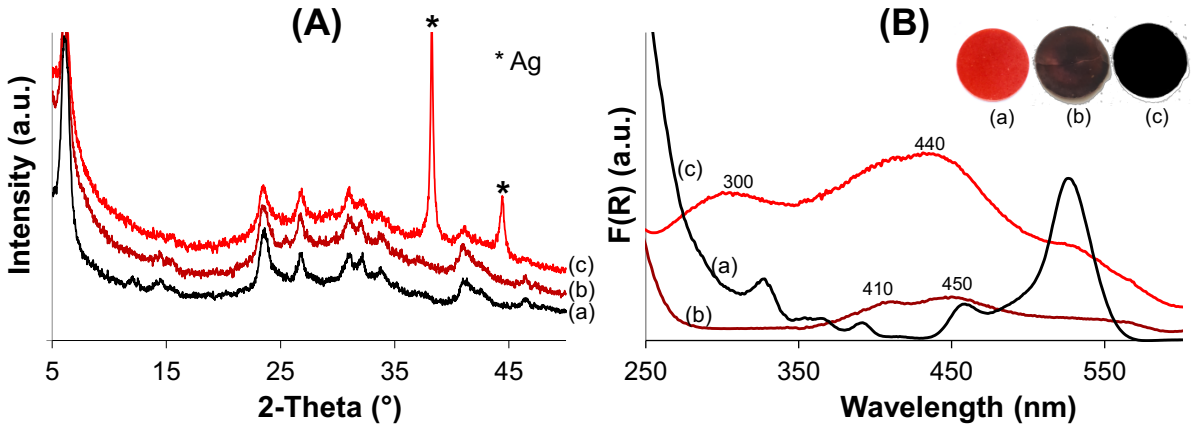

Figure 4. (A) X-ray diffractograms and (B) DR-UV-visible spectra of Ag/ZX-Bi: (a) as-prepared, (b) after activation at 200 °C under Ar and (c) then 12 h of the photocatalytic test. Reaction conditions: [MeOH]= 10350 ppm in 20%O_2/Ar; $m_{catalyst}$=20mg; Lampe Xe with filter pass high (λ>390nm); irradiance = 71 mW/cm^2; Total flow= 25 cm^3/min. Catalysts activated at 200 °C under Ar for 30 min in dark followed by 30 min under visible irradiation; heating rate = 2°C/min.

Fig. 4(A) shows that the diffraction pattern of Ag/ZX-Bi remains intact after activation at 200 °C under Argon, suggesting that the thermal treatment did not alter the catalyst structure or that the induced changes resulting from this treatment are below the detection limit of XRD and/or due the high dispersion of Ag with ultra small size particles. However, the Ag/ZX-Bi became brown-pink after heat treatment which induced significant changes in the DR-UV-Vis spectrum of the sample (spectrum b, Fig. 4(B)). Most of the bands in the UV region characteristic of hydrated and non-hydrated $Ag_n^{\delta+}$ clusters (with n>δ) embedded in the sodalite cages disappeared. Instead, a new broad absorption band, with two maxima at 410 and 450 nm,was observed in the visible region. These absorption bands are assigned to the presence of a metallic silver cluster with a small grain size that is uniformly distributed in/on the zeolite structure [21,23,24]. However, The XRD pattern recorded for Ag/ZX-Bi after 12 h of reaction time (Fig. 4(A)) shows two new diffraction peaks at 2Θ = 38.118 and 44.304 ° characteristic of (111) and (200) planes of Ag nanoparticles (AgNPs) (JCPDS file No. 5-2872) [33]. This is consistent with the color change of the pellet to dark-black, resulting in the broadening of the absorption spectrum in the visible region (spectrum c, Fig. 4(B)).

The two maxima centered at 300 and 440 nm are respectively attributed to the interbond resonance transitions of 4d-5s and the surface plasmon resonance (SPR) peak of AgNPs [34,35]. These results agree with the TEM analysis (Fig. 5). After activation, the sub-nanometer Ag species, visible as dark spots, migrate through the zeolite channels to the surface to forms AgNPs with an increased diameter from 1 to 4 nm (Fig. 5b). These particles of the Ag clusters are probably below the XRD detection limit. During methanol photooxidation, Ag NPs sintering with ~6 nm of diameter can be observed after 1 h of reaction (Fig. 5c) and become more pronounced after 12 h (Ag NPs diameter > 20 nm; Fig. 5d) of reaction. The same phenomenon was observed by Monpezat et *al.* [13] on Ag supported ZSM-5 upon thermal treatment from RT to 350 °C under nitrogen. The detailed sintering mechanism responsible for the growth of silver nanoparticles and the quantification of silver species that diffuse from the core to the surface of the zeolite crystals upon thermal treatment were studied by environmental high-angle annular dark-field scanning transmission electron microscopy (E-HAADF-STEM) combined with fast Electron Tomography (ET). The authors show that the sintering of silver particles occurs mainly through Ostwald ripening, a process that enables silver initially localized in the zeolite micropores and mesopores to reach the surface. This process starts at RT and increases with increasing the temperature of thermal treatment. To our knowledge, this phenomenon was not reported up to now during a photocatalytic process at room temperature. Howevere, this study reveals that Ostwald ripening can also take place during photocatalysis under visible light and at room temperature.

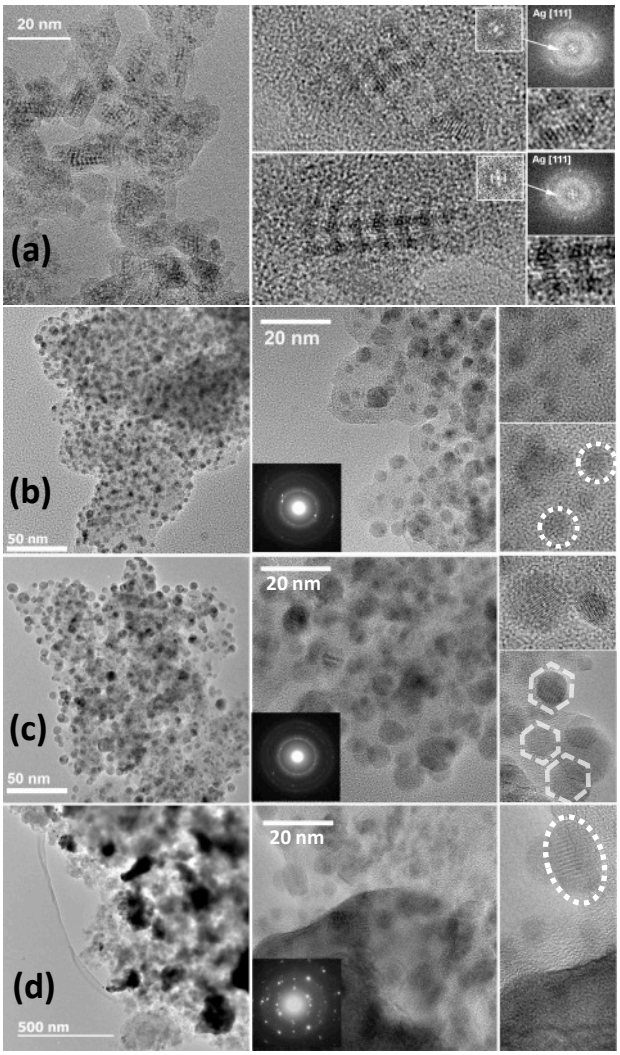

Figure 5. TEM images of: (a) the as-prepared Ag/ZX-Bi catalyst, (b) after activation at 200 °C under Argon, and of Ag@ZX-Bi_200 after (c) 1 and (d) 12 h of the photocatalytic tests. Reaction conditions: [MeOH]= 10350 ppm in 20%O_2/Ar; $m_{catalyst}$=20mg; Lampe Xe with filter pass high (λ>390nm); irradiance = 71 mW/cm^2; Total flow= 25 cm^3/min. Catalysts activated at 200 °C under Ar for 30 min in dark followed by 30 min under visible irradiation; heating rate = 2°C/min.

To conclude, the sintering of silver on Ag@ZX-Bi_200 becomes more pronounced upon performing the reaction under visible irradiation and reaction flow and that the increase of the reactant concentration accelerates this phenomenon. The correlation between the particle size of Ag (nm), the baseline intensity (deduced from the FTIR spectra of catalyst surface), and the MeOH conversion % during methanol photooxidation are reported in Fig. 6. It is clear that the catalytic activity of Ag/ZX-Bi catalyst is strongly dependent on the size distribution and dispersion of silver

species on the support. It decreases with reaction time due to the sintering of Ag clusters into larger metal nanoparticles. Thus, the maximum photocatalytic activity (53 % of MeOH conversion) was reached after 1 h of reaction, in which the Ag nanoparticles with an optimum size of ~6 nm are predominant.

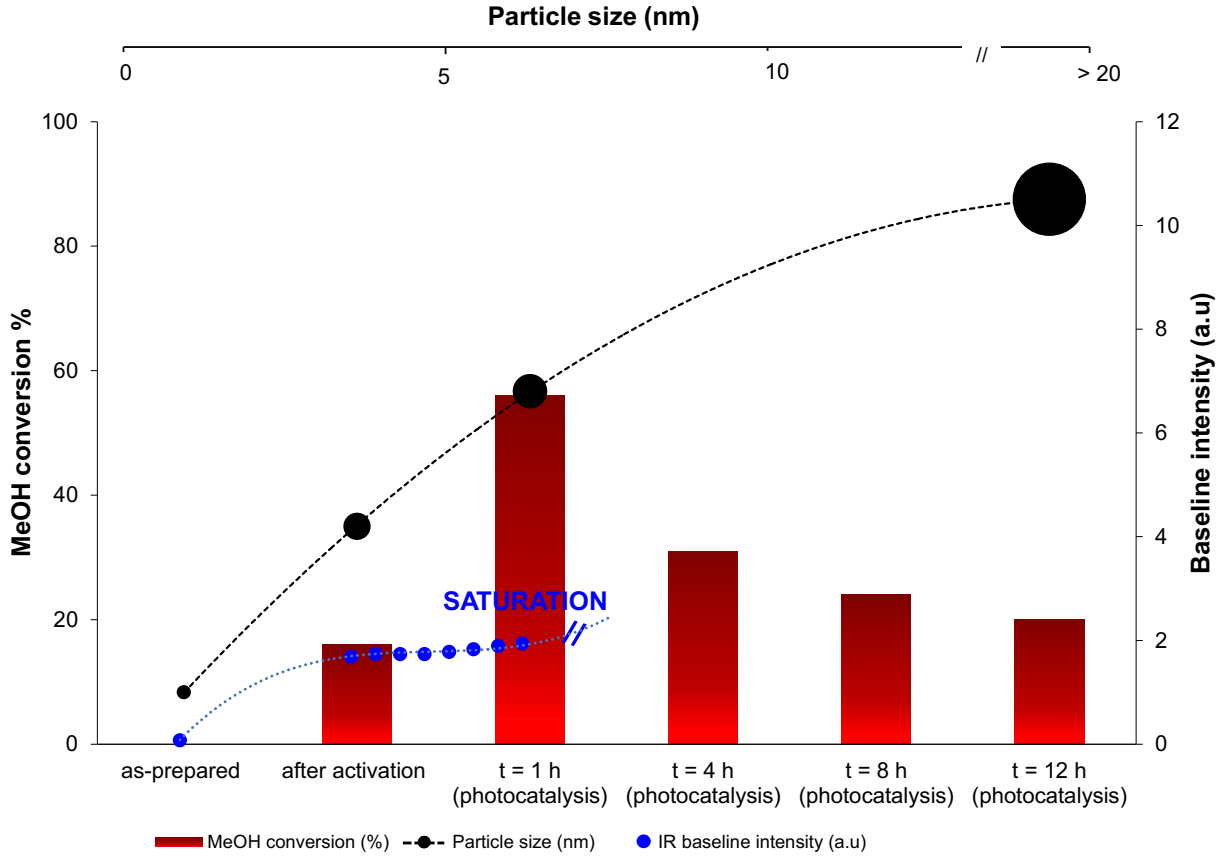

Figure 6. Correlation of MeOH conversion % with the particle size (nm) and the baseline intensity of the IR surface of Ag@ZX-Bi_NA and Ag@ZX-Bi_200 and of Ag@ZX-Bi_200 after various time of the photocatalytic tests under visible irradiation at RT. The as-prepared (Ag@ZX-Bi_NA) sample is added for comparison.

3.3. Reaction mechanism

The set of experimental data revealed that the Ag/ZX-Bi_NA predominant by the interconnected Ag NCs was very low active during the methanol photooxidation under visible light at RT, while Ag/ZX-Bi_200 with an Ag NPs size avearage around 6 nm exhibited the highest

activity in this reaction. This means that the local heating generated by the plasmonic effect of the silver-quasinanoparticles under visible light is not enough sufficient for intitiating the oxidation. In addition, the operando IR experminent reveals no significant bands intensities of possible reaction intermediates formed/adsorbed on the catalyst surface. This can be explained by an extremly high turnover frequency (TOF) or that the reaction take place in the gas phase by generating reactive oxydant species. To better understand the action mode of the Ag/ZX-Bi_NA and Ag/ZX-Bi_200 photocatalyst and highliting the reaction mechanism, additional experiments on the excited-state properties of both catalysts as well as the formation of reactive oxygen species were performed using the nanosecond time-resolved (Absorption transient) spectroscopy and the fluorescence emission of a probe molecule (i.e. 1,3-Diphenylisobenzofuran (DPBF)), respectively. In Figure 7(A), the absorption transient (AT) spectra of dispersed Ag/ZX-Bi_NA in water, after excitation at 532 nm, demonstrates bleaching in the region of 440-535 nm with an isosbestic point at 540 nm in agreement with the visible absorption spectra of this sample. An AT band can be observed with a maximum at 570 nm. This band can be assigned to a charge transfer between the Ag particles and their surroundings (e.g. zeolite). The lifetime of the AT (Fig. 7(B)) was found to be lower than the resolution limit of our technique (10 nm). By contrast, no AT was detected for the Ag/ZX-Bi_200. However, bleaching is observed in the visible range (more pronounced at 570 nm) with a life-time of around 1.8 μs (insert Fig. 7(B)), much more important than that detected with the non-activated sample. This long time of the AgNPs excitation is relatively enough for promoting therefore a chemical reaction or energy transfer between the molecule and the excited state while the short lifetime of Ag/ZX-Bi_NA is in agreement with the low photocatalytic activity of this sample. The Ag/ZX-Bi_NA showed fast water desorption for almost 80 % in the first three minutes of irradiation under visible light, as proved in our previous work [16]. The delay on the

water release (in minutes) is mainly due to the shading effect with an heteregeneous irradiation of the catalyst bed. Therefore, the low activity of this catalyst can be assigned to a very low lifetime of the generated charge, shorter than the diffusion of the reactant to the active sites as the Ag species are embedded in the zeolite cages and that the generated local temperature is not enough for promoting the oxidation.

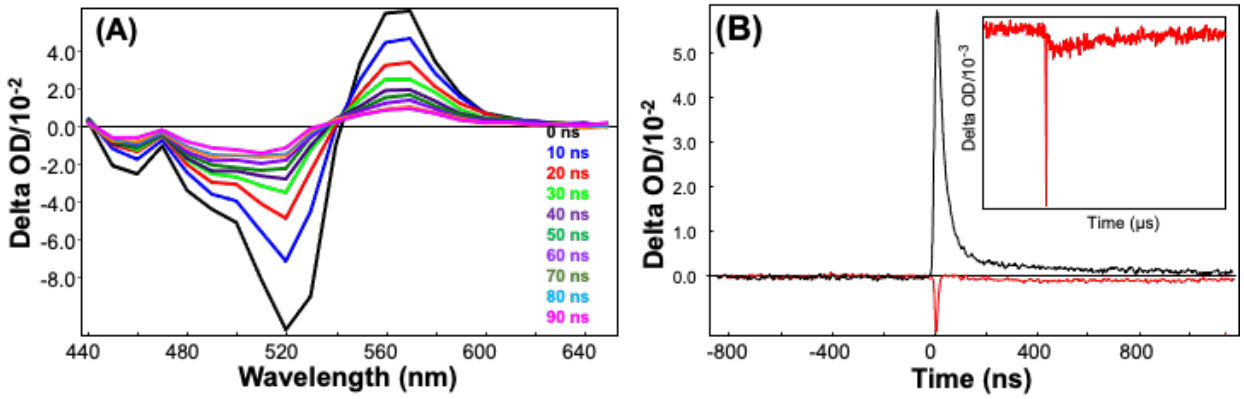

Figure 7. (A) Evolution of the absorption transient (AT) spectrum (0-10 ns) of the Ag/ZX-Bi_NA suspension (in water). (B) The kinetic decay, measured at 570 nm under air, of Ag/ZX-Bi_NA (black) and Ag/ZX-Bi_200 (red) suspensions (in water). Insert: the kinetic decay of Ag/ZX-Bi_200 registered for 6 µs after excitation. $\lambda_{excitation}$=532 nm.

Once the catalyst is activated, AgNPs are then formed on the zeolite surface, making the active site more accessible and the excited state livetime longer. Then, after Ag NPs excitation under visible irradiation, electrons of the 5sp band is be excited to the higher energy levels by intraband transition [36] . The LSPR effect led to the so-called “hot-electron” formation in the higher energy levels and left positively charged vacancies in the lower energy levels [36]. Then the oxidation reaction can be inititaed via two possible pathways: i) by electron transfer in which O_2 may capture the electrons with enough energy in the gas phase to form a superoxide radical anion ($O_2^{\bullet-}$) [37], or ii) by energy transfer from the excited state of silver particles under visible irradiation, enhanced by the LSPR effect, to O_2 molecules leading to the formation of the more reactive molecular triplet oxygen form such as the singlet oxygen (noted as $^1O_2$ or O_2 ($^1\Delta_g$)) [38,39,40,41]. Both reactive

oxygen species (ROS), i.e. superoxide radical anion and singlet oxygen, can be detected using the 1,3-Diphenylisobenzofuran (DPBF) as a probe molecule [17, 42,43,44,45]. In order to highlight the mechanism, the fluorescence of DPBF in presence of Ag/ZX-Bi_200 was examined as described in the experimental section and in reference [17]. The experiment was conducted under monochromatic visble light irradition (LED 405 nm) and different atmospheric conditions: i) under oxygen, ii) under argon and ii) under air. The results can be discussed qualitatively and the quantum yield of reactive oxygen species formation could not be determined due to the inhomogeneous dispersion of the solid catalyst in the n-heptane solution. The results are shown on Figure S12. A rapid and complete desappearence of DPBF fluorescence signal is observed after 30 seconds of irradiation under oxygen (spectrum (a), red), while it was almost unchanged under argon (spectrum (b), black). When this later is re-exposed to air (spectrum (c), blue), a significant decrease of the DPBF fluorescence signal is observed. This results shows without doubt the production of singlet oxygen and/or superoxide radical anion over Ag/ZX-Bi_200 catalyst under visible light (405 nm).

Based on that, the Ag/ZX-Bi_NA, its low activity could be attributed to its higher photoluminescence as well as to its lower excited state lifetime. However, the longer excited state lifetime in case of the Ag/ZX-Bi_200 is probably enough for promoting the reaction resulting in a plasmon-enhanced energy or electron transfer. A tentative transfer mechanism during the photooxidation of methanol over Ag/ZX-Bi_200 is illustrated in Scheme 2. The reaction pathway over Ag/ZX-Bi_200 contains three main steps: i) photoexcitation of Ag NPs under visible light and intraband transition of 5 sp electrons, ii) energy and/or electron transfer from LSPR of Ag NPs to molecular oxygen and thus formation of highly reactive singlet oxygen species ($^1O_2$) and/or

superoxide radical anion ($O_2^{\bullet-}$) and the iii) multistep oxidation of methanol and its subproducts by $^1O_2$ and/or $O_2^{\bullet-}$ to form CO_2 and H_2O.

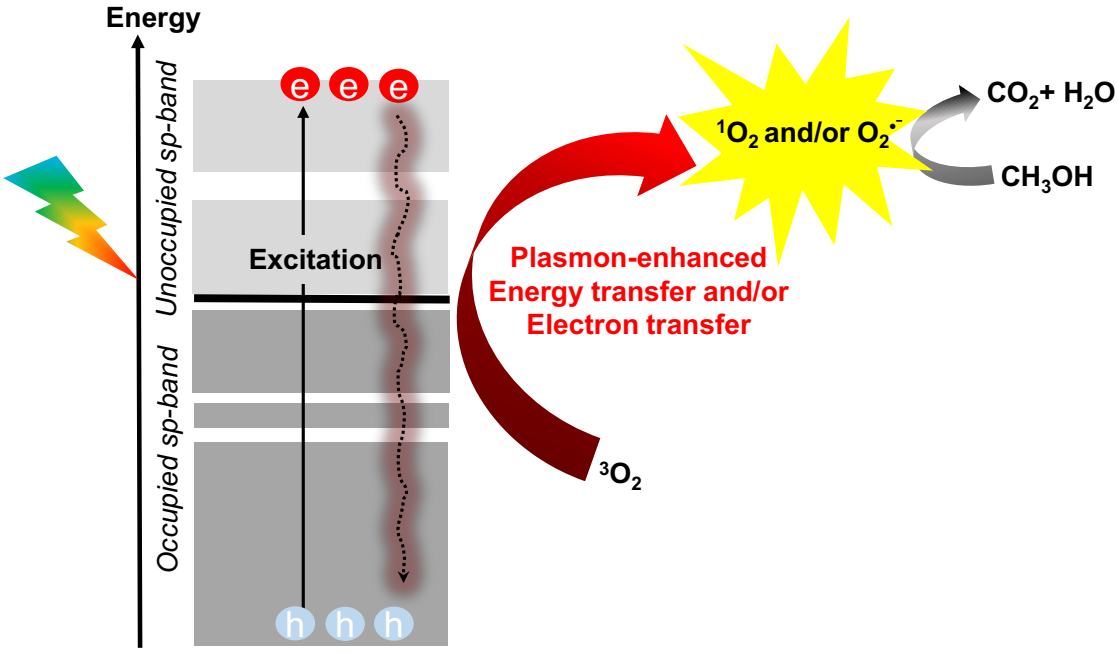

Scheme 2. The reaction patheway of Methanol photo-oxidation over Ag/ZX-Bi_200 under visible irradiation at RT.

4. Conclusion

In summary, sub-nanometer silver clusters based photocatalyst (Ag/ZX-Bi) were synthesized and evaluated during the photocatalytic oxidation of methanol under visible light at room temperature (T = 25 °C). The as-prepared Ag/ZX-Bi_NA was very low active during the methanol photooxidation. By contrast, the preactivation of the Ag/ZX-Bi at 200°C (Ag/ZX-Bi_200) had a synergetic enhancement of its photocatalytic activity (3.58 $mmol.g^{-1}.cm^{-2}$ corresponding to 57 % of MeOH conversion at t = 20 min) with high selectivity towards CO_2 (> 97%). This activity was explained by the migration and agglomeration of sub-nanosized $Ag_n^{\delta+}$ clusters into Ag nanoparticles with a size of 6 nm. With the evolution of reaction time, the catalyst experiences a

partial deactivation due to the formation of larger silver particles with > 20 nm of diameter. However, despite the deactivation, the catalyst is still 6 times more active than commercial TiO_2 (P25), used as reference, even after 12 h of reaction. Similar catalytic performance, but with substantially lower activity, were observed for a sample (IE-Ag/ZX-Bi_200) prepared by a simple ion-exchange and activation at 200°C. From a mechanistic point of view, the formation of singlet oxygen and/or superoxide radical anion in Ag/ZX-Bi_200 sample, enhanced by the LSPR effect of Ag nanoparticles, was confirmed by following the fluorescence of DPBF used as probe molecule. These reactive species can oxidize the methanol and its subproducts into CO_2 and H_2O. By contrast, the interconnected $Ag^{\delta+}$ nanoclusters, originally present in the as-prepared Ag/ZX-Bi-NA, show very low activity due to the short lifetime/low population of the triplet state. Based on that, the Ag@ZX-Bi_200 is a potential candidate in photocatalysis where the desactivation problem can be limited by working with softer reaction condition (lower methanol concentration, low irradiation intensity, etc.) as we demonstrate in our work.

ASSOCIATED CONTENT

Supporting Information.

In-situ adsorption of CO and TEM images of ZX-Bi and Ag/ZX-Bi catalysts and additional information of methanol conversion over all catalysts.

AUTHOR INFORMATION

Corresponding Author

***** *E-mail address: mohamad.elroz/ensicaen.fr*

Author Contributions

‡ These authors contributed equally. The manuscript was prepared written through the contributions of all authors. All authors have approved the final version of the manuscript.

ACKNOWLEDGMENT

Authors acknowledge the PHC Tassili program (17MDU983) and European Regional Development Fund (ERDF), Normandy region (H_2CO_2 project), for the financial support.

References

[1] Derikvandi, H., & Nezamzadeh-Ejhieh, A. A comprehensive study on enhancement and optimization of photocatalytic activity of ZnS and SnS2: Response Surface Methodology (RSM), nn heterojunction, supporting and nanoparticles study. *Journal of Photochemistry and Photobiology A: Chemistry*. **2017**, *348*, 68-78.

[2] Ghattavi, S., & Nezamzadeh-Ejhieh, A. GC-MASS detection of methyl orange degradation intermediates by AgBr/g-C_3N_4: Experimental design, bandgap study, and characterization of the catalyst. *International Journal of Hydrogen Energy*. **2020**, *45*(46), 24636-24656.

[3] Chai, O. J. H., Liu, Z., Chen, T., & Xie, J. Engineering ultrasmall metal nanoclusters for photocatalytic and electrocatalytic applications. *Nanoscale*. **2019**,11(43), 20437-20448.

[4] Derikvandi, H., Vosough, M., & Nezamzadeh-Ejhieh, A. A comprehensive study on the enhanced photocatlytic activity of a double-shell mesoporous plasmonic $Cu/Cu_2O/SiO_2$ as a visible-light driven nanophotocatalyst. *Environmental Science and Pollution Research*. **2020**, 27(22), 27582-27597.

[5] Mukherjee, S., Zhou, L., Goodman, A. M., Large, N., Ayala-Orozco, C., Zhang, Y., & Halas, N. J. Hot-electron-induced dissociation of H_2 on gold nanoparticles supported on SiO_2. *Journal of the American Chemical Society*. **2014**,136(1), 64-67.

[6] Mukherjee, S., Libisch, F., Large, N., Neumann, O., Brown, L. V., Cheng, J.? & Halas, N. J. Hot electrons do the impossible: plasmon-induced dissociation of H_2 on Au. *Nano letters*. **2013**, 13(1), 240-247.

[7] Christopher, P., Xin, H., Marimuthu, A., & Linic, S. Singular characteristics and unique chemical bond activation mechanisms of photocatalytic reactions on plasmonic nanostructures. *Nature materials*. **2012,** 11(12), 1044-1050.

[8] Christopher, P., Xin, H., & Linic, S. Visible-light-enhanced catalytic oxidation reactions on plasmonic silver nanostructures. *Nature chemistry*. **2011**, 3(6), 467-472.

[9] Sheikholeslami, S., Jun, Y. W., Jain, P. K., & Alivisatos, A. P. Coupling of optical resonances in a compositionally asymmetric plasmonic nanoparticle dimer. *Nano letters*. **2010,** 10(7), 2655-2660.

[10] Jain, P. K., & El-Sayed, M. A. Plasmonic coupling in noble metal nanostructures. *Chemical Physics Letters.* **2010,** 487(4-6), 153-164.

[11] Hao, E., & Schatz, G. C. Electromagnetic fields around silver nanoparticles and dimers. *The Journal of chemical physics*. **2004**, 120(1), 357-366.

[12] Derikvandi, H., & Nezamzadeh-Ejhieh, A. Increased photocatalytic activity of NiO and ZnO in photodegradation of a model drug aqueous solution: effect of coupling, supporting, particles size and calcination temperature. *Journal of hazardous materials*. **2017**, 321, 629-638.

[13] Monpezat, A., Topin, S., Thomas, V., Pagis, C., Aouine, M., Burel, L., & Roiban, L. Migration and growth of silver nanoparticles in Zeolite socony mobil 5 (ZSM-5) observed by environmental electron microscopy: Implications for heterogeneous catalysis. *ACS Applied Nano Materials*. **2019**, 2(10), 6452-6461.

[14] Santillán, J. M., Arboleda, D. M., Muraca, D., Schinca, D. C., & Scaffardi, L. B. Highly fluorescent few atoms silver nanoclusters with strong photocatalytic activity synthesized by ultrashort light pulses. *Scientific Reports*. **2020**, 10(1), 1-13.

[15] Li, K., Hogan, N. J., Kale, M. J., Halas, N. J., Nordlander, P., & Christopher, P. Balancing near-field enhancement, absorption, and scattering for effective antenna–reactor plasmonic photocatalysis. *Nano letters*, **2017**, 17(6), 3710-3717.

[16] Douma F., lakissa L., Lebedevb O., Cardin J., Kostovd K.L., El Fallaha J., Valtcheva V., El-Roz. M. Silver quasi-nanoparticles: bridging the gap between clusters molecular-like and plasmonic nanoparticles, *The Royal Society of Chemistry*. **2021,** 00 1-3.DOI 10.1039/D1MA00382H.

[17] Monadjemi S., El Roz m., Richard C. & Ter Halle A., Photoreduction of chlorothalonil fungicide on plant leaf models, *Environmental science & technology*. **2011**, *45,* 9582-9589.

[18] El-Roz, M., Kus, M., Cool, P., & Thibault-Starzyk, F. New operando IR technique to study the photocatalytic activity and selectivity of TiO_2 nanotubes in air purification: influence of temperature, UV intensity, and VOC concentration. *The Journal of Physical Chemistry C*. **2012**, 116(24), 13252-1326.

[19] El-Roz, M., Bazin, P., & Thibault-Starzyk, F. An operando-IR study of photocatalytic reaction of methanol on new* BEA supported TiO_2 catalyst. *Catalysis today*. 2013 205, 111-119.

[20] Treacy, M. M., & Higgins, J. B. **2007**. Collection of simulated XRD powder patterns for zeolites fifth (5th) revised edition. Elsevier.

[21] Gurin, V. S., Bogdanchikova, N. E., & Petranovskii, V. P. Few-atomic silver clusters in zeolites: Ab initio MO LCAO calculation and optical spectroscopy. *The Journal of Physical Chemistry B*. **2000**, 104(51), 12105-12110.

[22] Tuzovskaya, I., Bogdanchikova, N., Pestryakov, A., Gurin, V., Simakov, A., & Lunin, V. Comparison of gold and silver species supported and incorporated into mordenites. *Advances in the Understanding and Application of Catalysts*. **2003,** 248.
[23] Fron, E., Aghakhani, S., Baekelant, W., Grandjean, D., Coutino-Gonzalez, E., Van der Auweraer, M., & Hofkens, J. Structural and photophysical characterization of Ag clusters in LTA zeolites. *The Journal of Physical Chemistry*. **2019**, 123(16), 10630-10638.
[24] Seifert, R., Rytz, R., & Calzaferri, G. Colors of Ag^{+}-exchanged zeolite A. *The Journal of Physical Chemistry A*. **2000**, 104(32), 7473-7483.
[25] El-Roz, M., Bazin, P., Daturi, M., & Thibault-Starzyk, F. On the mechanism of methanol photooxidation to methylformate and carbon dioxide on TiO_2: an operando-FTIR study. *Physical Chemistry Chemical Physics*. **2015**, 17(17), 11277-11283.
[26] Ejhieh, A. N., & Khorsandi, M. Photodecolorization of Eriochrome Black T using NiS–P zeolite as a heterogeneous catalyst. *Journal of Hazardous Materials*. **2010**, 176(1-3), 629-637.
[27] Cavicchioli, M.; Varanda, L. C.; Massabni, A. C.; Melnikov, P. Silver nanoparticles synthesized by thermal reduction of a silver(I)−aspartame complex in inert atmosphere. *Materials Lett*ers. **2005**, 28, 3585− 3589.
[28] Ftouni K., Lakiss L., Thomas S., Daturi M., Fernandez C., Bazin P., ... & El-Roz M., TiO_2/Zeolite Bifunctional (Photo) catalysts for a selective conversion of methanol to dimethoxymethane: on the role of brønsted acidity. *The Journal of Physical Chemistry C*. **2018**, 122, 29359-29367. https://doi.org/10.1021/acs.jpcc.8b10092.
[29] Han, C., Yang, X., Gao, G., Wang, J., Lu, H., Liu, J., ... & Liang, X. Selective oxidation of methanol to methyl formate on catalysts of Au–Ag alloy nanoparticles supported on titania under UV irradiation. *Green Chemistry*. **2014**, *16*(7), 3603-3615..
[30] Kaminski, P. The application of FTIR in situ spectroscopy combined with methanol adsorption to the study of mesoporous sieve SBA-15 with cerium-zirconium oxides modified with gold and copper species. *Arabian Journal of chemistry*. **2020**. *13*(1), 851-862.
[31] Bezverkhyy, I., Bouguessa, K., Geantet, C., & Vrinat, M. Adsorption of tetrahydrothiophene on faujasite type zeolites: Breakthrough curves and FTIR spectroscopy study. *Applied Catalysis B: Environmental*. **2006**, *62*(3-4), 299-305.
[32] Kohler, A., Sulé-Suso, J., Sockalingum, G. D., Tobin, M., Bahrami, F., Yang, Y., ... & Martens, H. Estimating and correcting Mie scattering in synchrotron-based microscopic Fourier transform infrared spectra by extended multiplicative signal correction. *Applied spectroscopy*. **2008**, 62(3), 259-266.
[33] Yang, H., Ren, Y. Y., Wang, T., & Wang, C. Preparation and antibacterial activities of $Ag/Ag^{+}/Ag^{3+}$ nanoparticle composites made by pomegranate (Punica granatum) rind extract. *Results in physics*. **2016**, 6, 299-304.
[34] Fares, H., Santos, S. N. C., Santos, M. V., Franco, D. F., Souza, A. E., Manzani, D., & Nalin, M. Highly luminescent silver nanocluster-doped fluorophosphate glasses for microfabrication of 3D waveguides. *RSC advances*. **2017**, 7(88), 55935-55944.
[35] Seo, J. T., Yang, Q., Kim, W. J., Heo, J., Ma, S. M., Austin, J., ... & Temple, D. Optical nonlinearities of Au nanoparticles and Au/Ag coreshells. *Optics letters*. **2009**, 34(3), 307-309.
[36] Chen, X., Zheng, Z., Ke, X., Jaatinen, E., Xie, T., Wang, D., ... & Zhu, H. Supported silver nanoparticles as photocatalysts under ultraviolet and visible light irradiation. *Green Chemistry*. **2010** 12(3), 414-419.
[37] Jones, A. M., Garg, S., He, D., Pham, A. N., & Waite, T. D. Superoxide-mediated formation and charging of silver nanoparticles. *Environmental science & technology.* **2011**, *45*(4), 1428-1434.
[38] Hu, B., Cao, X., Nahan, K., Caruso, J., Tang, H., & Zhang, P Surface plasmon-photosensitizer resonance coupling: an enhanced singlet oxygen production platform for broad-spectrum photodynamic inactivation of bacteria. *Journal of Materials Chemistry B*. **2014**, 2(40), 7073-7081.
[39] Vankayala, R., Sagadevan, A., Vijayaraghavan, P., Kuo, C. L., & Hwang, K. C. Metal nanoparticles sensitize the formation of singlet oxygen. *Angewandte Chemie International Edition*. **2011**, 50(45), 10640-10644.
[40] Hamoud, H. I., Lafjah, M., Douma, F., Lebedev, O. I., Djafri, F., Valchev, V., & El-Roz, M. Photo-assisted SCR over highly dispersed silver sub-nanoparticles in zeolite under visible light: An Operando FTIR study. *Solar Energy*. **2019**, 189, 244-253.
[41] Planas, O., Macia, N., Agut, M., Nonell, S., & Heyne, B. Distance-dependent plasmon-enhanced singlet oxygen production and emission for bacterial inactivation. *Journal of the American Chemical Society*. **2016**, 138(8), 2762-2768.
[42] Ohyashiki, T., Nunomura, M., & Katoh, T. Detection of superoxide anion radical in phospholipid liposomal membrane by fluorescence quenching method using 1, 3-diphenylisobenzofuran. *Biochimica et Biophysica Acta (BBA)-Biomembranes*. **1999,** *1421*(1), 131-139.

[43] Wang, K. K., Song, S., Jung, S. J., Hwang, J. W., Kim, M. G., Kim, J. H., ... & Kim, Y. R. Lifetime and diffusion distance of singlet oxygen in air under everyday atmospheric conditions. *Physical Chemistry Chemical Physics*. **2020**, *22*(38), 21664-21671.
[44] Ho-Wu, R., Yau, S. H., & Goodson III, T. Efficient singlet oxygen generation in metal nanoclusters for two-photon photodynamic therapy applications. *The Journal of Physical Chemistry B*. **2017**, *121*(43), 10073-10080.
[45] Chadwick, S. J., Salah, D., Livesey, P. M., Brust, M., & Volk, M. Singlet oxygen generation by laser irradiation of gold nanoparticles. *The Journal of Physical Chemistry C*. **2016**, *120*(19), 10647-10657.